Hydroxyl combined with nitrogen on biomass carbon promotes the electrocatalytic H$_2$O$_2$ selectivity

Jiabi JIANG[1], Danni DENG[1], Yuchao WANG[1], Yingbi CHEN[1], Yu BAI[1], Meng WANG[1], Xiang XIONG[1], and Yongpeng LEI[1,*]

[1] *State Key Laboratory of Powder Metallurgy, Central South University, Changsha, Hunan, 410083, China*

*Corresponding author e-mail: leiyongpeng@csu.edu.cn

Abstract

Elevating the selectivity of two-electron oxygen reduction reaction (2e$^-$ ORR) is challenging. Herein, the hydroxyl combined with nitrogen on biomass carbon exhibits a high H$_2$O$_2$ selectivity over a wide potential range of 0 V to 0.5 V vs. RHE, which is nearly 97% at 0.3 V vs. RHE. The combination of hydroxyl and nitrogen improves the adsorption and desorption of intermediates, finally changing the reaction pathway and promoting the selectivity of 2e$^-$ ORR. The Faradaic efficiency (FE) reaches 98% at 0.3 V vs. RHE. Furthermore, the typical organic pollutants were degraded on site in flow cell. This work illustrates the potential of biomass carbon in 2e$^-$ ORR.

1. Introduction

The electrochemical two-electron oxygen reduction reaction (2e$^-$ ORR) is a potential strategy to produce H$_2$O$_2$ on site under mild conditions [1,2]. However, due to the slow kinetic process of 2e$^-$ORR and the competition of 4e$^-$ ORR, the low reactivity and unsatisfactory H$_2$O$_2$ selectivity need to be overcome [3,4]. The weaknesses of high cost, poor chemical stability and scarcity limit the use of precious metal materials (e.g., Au, Pt, Pd, and Pd-Au) [5,6,7]. Besides, the limited active site is the disadvantage of single-atom catalysts [8,9].

Due to sustainability, simple synthesis, and low cost, biomass carbon shows potential for 2e$^-$ ORR [10,11]. The construction of efficient active sites on carbon catalysts through the introduction of functional groups [12], heteroatom doping [13,14] and defect engineering [15,16], have proved to be effective to change the ORR pathway (O$_2$→*OOH→HO$_2^-$). The oxygen-containing functional groups on carbon dots were precisely regulated to achieve the 2e$^-$ ORR pathway [17]. In this work, the biomass carbon containing hydroxyl and nitrogen (HNC) displayed high H$_2$O$_2$ selectivity (97% at 0.3 V vs. RHE) for 2e$^-$ ORR. The FE reached 98% at 0.3 V vs. RHE. Further, the typical organic pollutants were degraded in flow cell, such as tetracycline (TC), rhodamine B (RhB) and methylene blue (MB).

2. Experimental

Materials: Chitosan (CTS) and Carboxylated cellulose nanofibers (CCN) were directly obtained from Macklin Inc Co., Ltd. Potassium hydroxide (KOH) and Sulfuric Acid were purchased from Sinopharm Chemical Reagent Co., Ltd. All aqueous solutions were prepared using deionized water obtained from Milli-Q ultrapure water (Millipore, ≥18.2 MΩ cm^{-1}). All of the reagents were of analytical grade (AR), and used without further purification.

Synthesis of samples: 1.0 g of CTS was placed in the porcelain boat, which was covered to prevent excessive loss during the pyrolysis process. After that, this porcelain boat was put in a tube furnace, and the temperature was raised to 500℃ at a rate of 5℃·min^{-1} under a nitrogen atmosphere. The high temperature was maintained for 3 h for pyrolysis. After it was naturally cooled and ground, the HNC catalyst can be obtained. The catalyst products at different pyrolysis temperatures were also prepared here. Except that the pyrolysis temperature was changed to 400℃, 600℃ and 700℃, the samples obtained without other preparation conditions were named HNC-400, HNC-600 and HNC-700. The preparation method of HC was similar to HNC, except that the raw material was CCN.

3. Results and discussion

A one-step heat treatment for CTS was conducted to obtain the biomass carbon containing hydroxyl and nitrogen (denoted as HNC). The synthetic route was illustrated in Figure 1(a). As seen from the scanning electron microscopy (SEM), HNC exhibited a large and thick irregular bulk structure (Figure 1(b)). The energy-dispersive X-ray spectroscopy (EDS) elemental mapping images reveal the existence and uniform distribution of C, O and N elements in HNC (Figure 1(c)). For comparison, the other biomass carbon from CCN without nitrogen was also prepared (denoted as HC). The preparation

method was same. SEM images show that the HC appeared fibrous and disorganized (Figure S1(a,b)). EDS elemental mapping images reveal that the C and O elements were homogeneously distributed in HC (Figure S1(c)). The contact angles for the HNC and HC were measured to be 123° and 63°, respectively (Figure 1(d)) [18]. The hydrophobicity exhibited by HNC was beneficial for the mass transfer process of O_2, thereby enhancing the performance of electrochemical synthesis of H_2O_2.

The structural detail of functional groups in these samples could be verified by Fourier transform infrared spectroscopy (FTIR). As displayed in Figure 1(e), the spectra of HNC and HC exhibited a wide peak at around 3422 cm^{-1}, which was mainly assigned to the stretching vibration of the adsorbed water [19-21]. The small peak at 3240 cm^{-1} of HNC could be attributed to the stretching vibration of N–H, which demonstrated the existence of amino functional groups [22,23]. The asymmetric stretching vibration peak of C–N bond was also discovered at 1414 cm^{-1}. The common peaks located at 2930 cm^{-1} and 868 cm^{-1} were vested in the stretching vibration of C–H. The strong peak of HC at 1445 cm^{-1} was considered to the bending vibration of O–H in carboxylic acid [24,25]. The peak located at 1680 cm^{-1} was attributed to the asymmetric stretching of C=C bonds. Besides, in the fingerprint region, HNC and HC exhibited a stretching vibration peak (1150 cm^{-1}) corresponding to C–OH and C–O-C groups.

The X-ray photoelectron spectroscopy (XPS) was further used to illustrate the surface chemical composition [26-28]. HNC was composed of C, O and N, whose contents were 79.3, 11.4 and 9.3 at%, respectively, while HC only contained C (76.2 at%) and O (23.8 at%) elements (Figure S2 and Table S1). These were consistent with EDS elemental mapping images. The C 1s spectrum of HNC displays three peaks at 284.8, 285.8 and 290.0 eV, corresponding to the C=C (68.8%), C-O/C-N (20.8%) and π-π* (10.4%), respectively (Figure 2(a)) [29,30]. Similarly, the HC, HNC-600 and HNC-700 display three peaks at nearby locations.
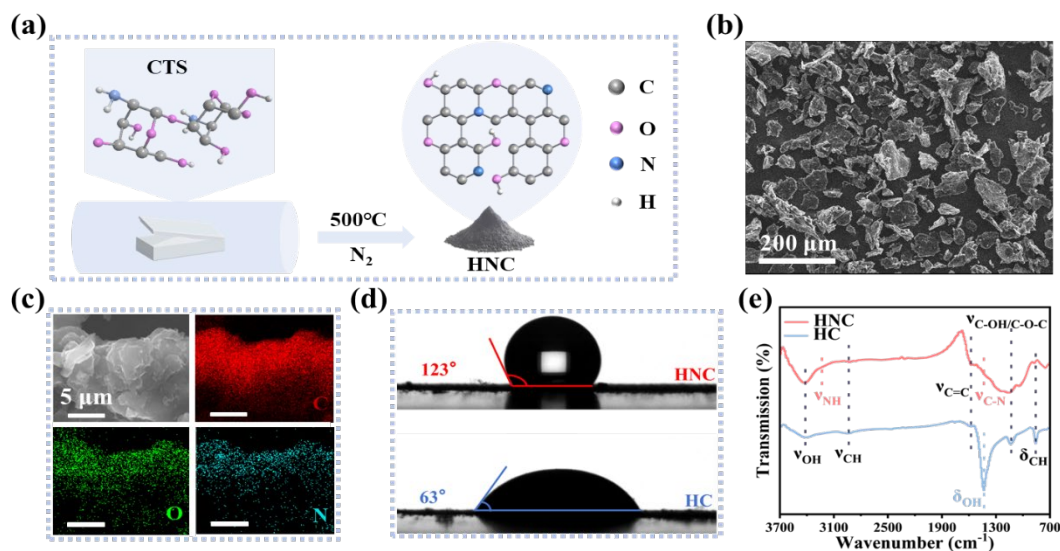

Figure 1. Synthesis and characterization. (a) Synthesis scheme, (b) SEM image, (c) EDS elemental mapping of HNC, (d) Contact angle tests, and (e) FTIR spectra of HNC and HC.
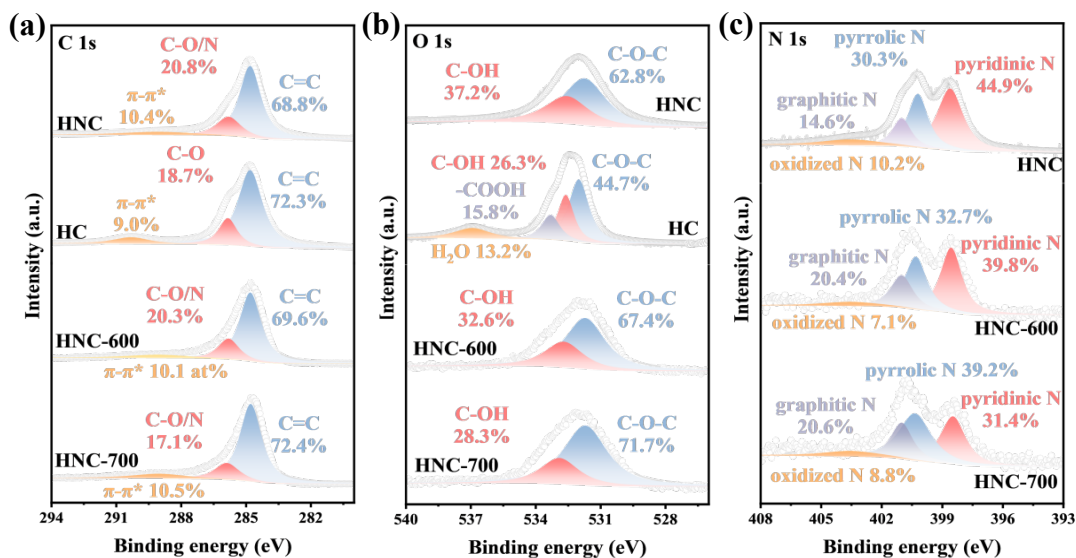

Figure 2. XPS spectra of different samples. High-resolution XPS spectra of (a) C 1s, (b) O 1s, and (c) N 1s.

The O 1s spectrum was fitted to distinguish the different surface oxygenic functional groups (Figure 2(b)). For HNC, two main O–containing species existed, namely C–O–C (531.7 eV) and C–OH (532.5 eV) [31]. Among them, the content of C–O–C and C–OH was 62.8% and 37.2%, respectively. The HC also showed two peaks of C–O–C (44.7%) and C–OH (26.3%) at similar positions. In addition, two peaks appeared at 533.3 eV and 536.9 eV according to –COOH (15.8%) and H_2O (13.2%), respectively [32,33]. These results were in good agreement with that of FTIR. The O 1s spectra of HNC-600 and HNC-700, which were mainly identified as two different regions, namely C–O–C and C–OH that were similar to HNC. With the increase of annealing temperature, the C–OH content of the three samples decreased, and the hydrogen peroxide selectivity of them showed the same rule in the subsequent test. Due to the fact that hydroxyl led to a weak oxygen (*O) adsorption tendency, it is inferred that C–OH was beneficial to the selectivity of two-electron path in electrocatalytic ORR in HNC [34].

The N 1s spectrum of HNC illustrates four peaks at 398.6, 400.2, 401.0, and 403.5 eV, corresponding to pyridinic N (44.9%), pyrrolic N (30.3%), graphitic N (14.6%) and oxidized N (10.1%), respectively (Figure 3(c)) [35-37]. With the increase of annealing temperature, the content of pyridinic N decreased, which was consistent with the rule of electrochemical test results, while the change law of pyrrolic N content was opposite. It is reasonable to suppose that pyridinic N provides an important active site for HNC, as the negative electrostatic charge of nitrogen could activate the adjacent positively charged carbon atoms, thus facilitating the proper adsorption of *OOH intermediate [38].

The defect distribution of HNC and HC was studied using Raman spectroscopy. The I_D/I_G of two samples indicated defective structures (Figure S3). The value of HC was smaller than HNC, indicating that nitrogen doping increased the degree of disorder, which was consistent with the XPS. In addition, the Zeta potential values of HNC and HC were both negative, corresponding to –4.3 mV and –14.0 mV, respectively (Figure S4). This indicates that the surface of both was negatively charged, which was conducive to the adsorption of H^+ in the solution, and accelerated the combination with reactive oxygen specie to form H_2O_2 [39-41]. The Zeta potential of HC was more negative, which maybe due to the more electronegative O element on its surface. The result agrees well with that of XPS results [42].

The Cyclic voltammetry (CV) curve of HNC had an evident reduction peak when the electrolyte was saturated with O_2, the reduction peak disappeared when N_2 was saturated, indicating that HNC responded to oxygen reduction. Other samples also had the same oxygen reduction responses (Figure S5). The electrocatalytic performance for 2e⁻ ORR was tested by using a standard rotating ring disk electrode (RRDE) in 0.1 M KOH. Before test, experiments using a ferrocyanide/ ferricyanide redox reaction system determined the collection efficiency of RRDE to be about 0.36 (Figure S6). The linear sweep voltammetry (LSV) curves of different samples collected at 1600 rpm were presented in Figure 3(a). HNC and HC exhibited similar curve shapes and current densities, suggesting that both have similar ORR activity. The HNC delivered a high H_2O_2 selectivity over 92% in a wide potential range (0 V to 0.5 V vs. RHE) with a maximum value of up to 97% (0.3 V vs. RHE), higher than that of HC (Figure 3(b)). Similarly, the electron transfer number (n) for HNC was calculated, with an average of 2.1 (0 V to 0.5 V vs. RHE), meaning that this was an almost complete 2e⁻ ORR process (Figure 3(c)). The double-layer capacitance (C_{dl}) of HNC and HC was calculated to be 0.256 mF·cm⁻² and 0.214 mF·cm⁻², respectively (Figure S7). Moreover, two samples showed similar Tafel slopes (Figure S8). These results are attributed to C–OH groups and pyridinic N on the biomass carbon which leads to proper adsorption of *OOH intermediate [43-45].
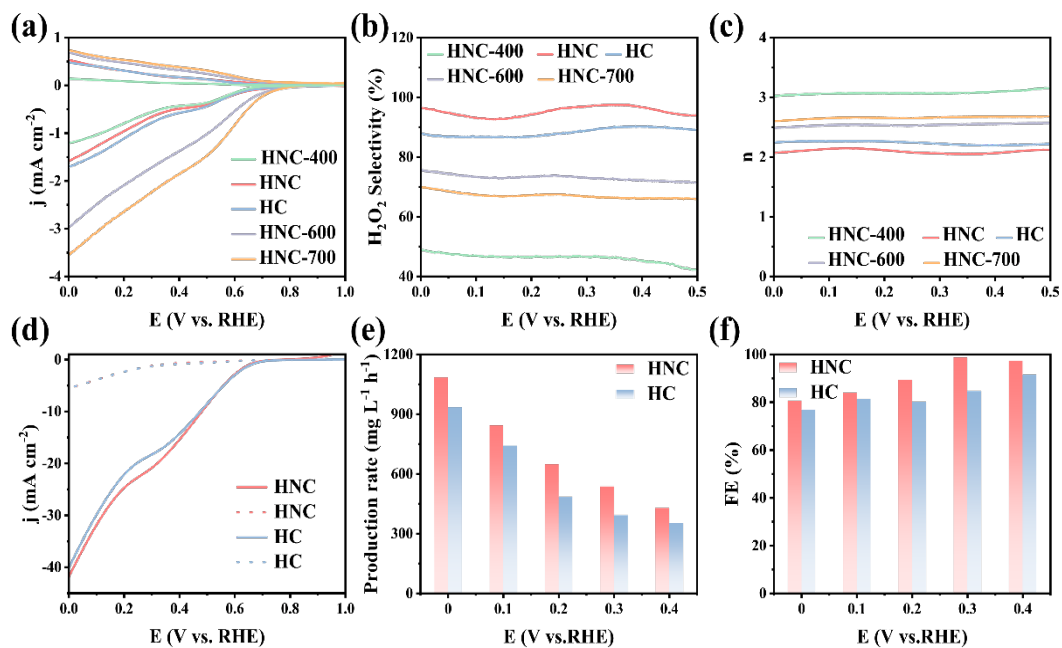

Figure 3. Electrocatalytic 2e⁻ ORR activity and H_2O_2 production performance in flow cell. (a) LSV curves of RRDE measurement at a scan rate of 5 mV·s⁻¹ and 1600 rpm in O_2 saturated 0.1 M KOH, (b) The calculated H_2O_2 selectivity, (c) n, (d) LSV curves of flow cell test in 1 M KOH (The dashed lines were tested under Ar conditions), (e) H_2O_2 production rate, and (f) FE.
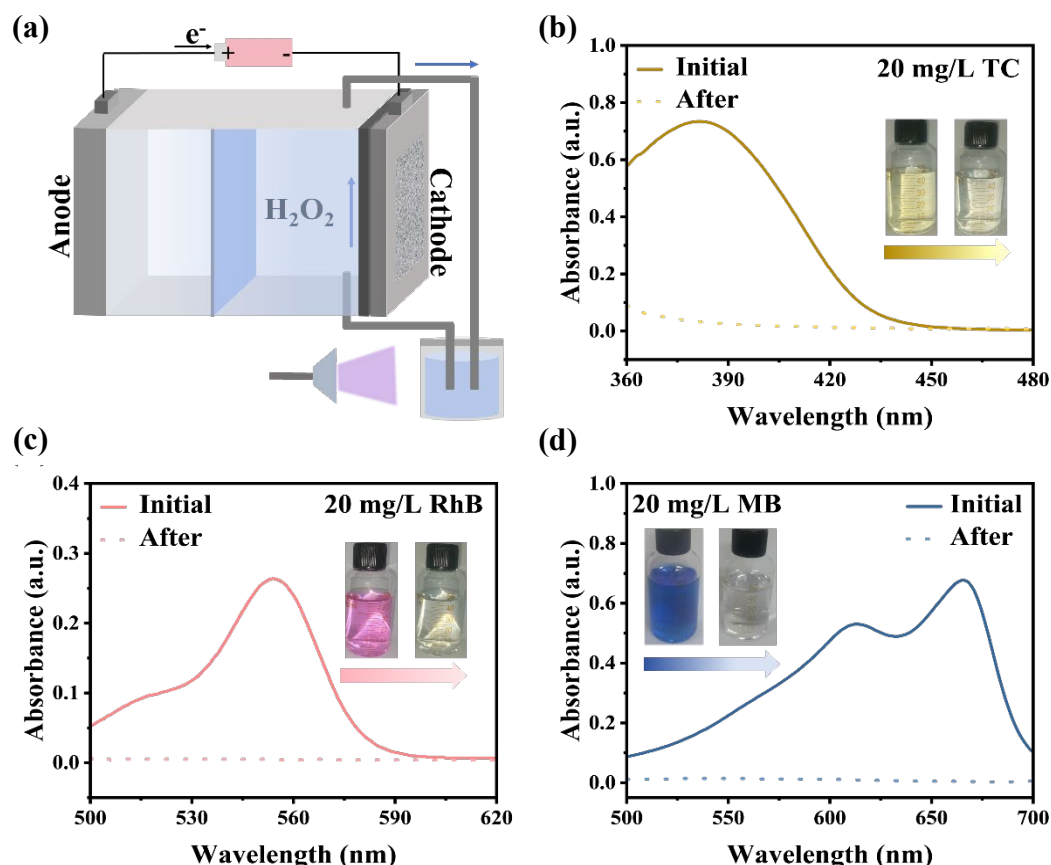
Figure 4. Pollutant degradation experiment. (a) Schematic illustration of UV/H_2O_2 coupled degradation systems. The UV-vis spectra of (b) TC, (c) RhB and (d) MB solution before and after degradation (The inset shows the photos of the TC, RhB and MB solution before and after degradation).

As known, the H_2O_2 yield was limited by the low solubility of O_2 in aqueous condition and mass transport. Hence, the three-phase flow cell reactor was further assembled to improve the H_2O_2 yield. A schematic diagram of the device and its optical photograph were shown in Figure S9. The LSV curves of HNC and HC recorded in flow cell containing the Air-saturated electrolyte exhibited a significant increase in the current density compared with that achieved in the Ar-feeding electrolyte, implying the occurrence of $2e^-$ ORR catalyzed by HNC/HC (Figure 3(d)).

The chronoamperometry tests were conducted and the H_2O_2 product was quantitatively determined by the ultraviolet-visible (UV-vis) spectroscopy (Figure S10). The HNC exhibited a gradual increase of the H_2O_2 production rate with the negative shift of working potential and achieves the maximal value of 1083 mg·L^{-1}·h^{-1} at 0 V vs. RHE (Figure 3(e)). As shown in Figure 3(f), the H_2O_2 FE of the HNC is over 80% (0 V to 0.4 V vs. RHE) and the highest FE is 98% (0.3 V vs. RHE). It is worth mentioning that the H_2O_2 production rate and FE of HNC were higher than HC, indicating a higher activity and selectivity in $2e^-$ ORR. This is in agreement with the result of the RRDE test.

The FE maintained above 80% and the activity as manifested by the current density showed little decay after 12 h continuous chronoamperometric measurement at 0.1 V (Figure S11). Furthermore, the potential of generated H_2O_2 on site to degrade organic pollutants was demonstrated (Figure 4(a)). Keeping the working electrode at a constant potential of 0 V vs. RHE and the illumination of the UV

lamp [46-48], TC solution completely degraded to colorless after 9 h (Figure 4(b)), RhB solution completely degraded to colorless after 4 h (Figure 4(c)), and MB solution completely degraded to colorless after 6 h (Figure 4(d)).

4. Conclusions

The HNC displays high H_2O_2 selectivity (nearly 97% at 0.3 V vs. RHE) and FE. The hydroxyl combined with nitrogen on biomass carbon is conducive to the proper adsorption of *OOH intermediate and improves the selectivity of electrocatalytic H_2O_2. Besides, the generated H_2O_2 degrade TC, RhB and MB in flow cell on site. This work demonstrates the potential of biomass carbon in the production of H_2O_2 through $2e^-$ ORR for organic pollutants.

References

[1] X. Zhou, Y. Min, C. Zhao, C. Chen, M.-K. Ke, S.-L. Xu, J.-J. Chen, Y. Wu, and H.-Q. Yu, "Constructing sulfur and oxygen super-coordinated main-group electrocatalysts for selective and cumulative H_2O_2 production," *Nature Communications*, vol. 15, p. 193, 2024.

[2] L. Sun, X. Jin, T. Su, A. C. Fisher, and X. Wang, "Conjugated nickel phthalocyanine derivatives for heterogeneous electro-catalytic H_2O_2 synthesis," *Advanced Materials*, vol. 36, no. 17, p. 2306336, 2024.

[3] H. Yang, N. An, Z. Kang, P. W. Menezes, and Z. Chen, "Understanding advanced transition metal-based two electron oxygen reduction electrocatalysts from the perspective of phase engineering," *Advanced Materials*, vol. 36, no. 25, p. 2400140, 2024.

[4] M. Mazzucato, A. Facchin, M. Parnigotto, and C. Durante, "New and revised aspects of the electrochemical synthesis of hydrogen peroxide: from model electrocatalytic systems to scalable materials," *ACS Catalysis*, vol. 14, no. 9, pp. 6369-6403, 2024.

[5] Z. Deng, A. H. B. Mostaghimi, M. Gong, N. Chen, S. Siahrostami, and X. Wang, "Pd 4d orbital overlapping modulation on Au @Pd nanowires for efficient H_2O_2 Production," *Journal of the American Chemical Society*, vol. 146, no. 4, pp. 2816-2823, 2024.

[6] Y. Zhang, Z. H. Lyu, Z. Chen, S. Zhu, Y. Shi, R. Chen, M. Xie, Y. Yao, M. Chi, M. Shao, and Y. Xia, "Maximizing the catalytic performance of $Pd@Au_xPd_{1-x}$ nanocubes in H_2O_2 production by reducing shell thickness to increase compositional stability," *Angewandte Chemie International Edition*, vol. 60, no. 36, pp. 19643-19647, 2021.

[7] H. Li, P. Wen, D. S. Itanze, Z. D. Hood, S. Adhikari, C. Lu, X. Ma, C. Dun, L. Jiang, D. L, Y. Qiu, and S. M. Geyer, "Scalable neutral H_2O_2 electrosynthesis by platinum diphosphide nanocrystals by regulating oxygen reduction reaction pathways," *Nature Communications*, vol. 11, p. 3928, 2020.

[8] C. Jia, Q. Sun, R. Liu, G. Mao, T. Maschmeyer, J. J. Gooding, T. Zhang, L. Dai, and C. Zhao, "Challenges and opportunities for single-atom electrocatalysts: from lab-scale research to potential industry-level applications," *Advanced Materials*, vol. 36, no. 42, p. 2404659, 2024.

[9] K.-Y. Chen, Y.-X. Huang, R.-C. Jin, and B.-C. Huang, "Single atom catalysts for use in the selective production of hydrogen peroxide via two-electron oxygen reduction reaction: mechanism, activity, and structure optimization," *Applied Catalysis B: Environmental*, vol. 337, no. 15, p. 122987, 2023.

[10] M. Gao, Z.-Y. Wang, Y.-R. Yuan, W.-W. Li, H.-Q. Liu, and T.-Y. Huang, "Ball-milled biochar for efficient neutral electrosynthesis of hydrogen peroxide," *Chemical Engineering Journal*, vol. 434, no. 15, p. 134788, 2022.

[11] Z. Luo, M. Liu, D. Tang, Y. Xu, H. Ran, J. He, K. Chen, and J. Sun, "High H_2O_2 selectivity and enhanced Fe^{2+} regeneration toward an effective electro-fenton process based on a self-doped porous biochar cathode," *Applied Catalysis B: Environmental*, vol. 315, no. 15, p. 121523, 2022.

[12] M. Fan, Z. Wang, K. Sun, A. Wang, Y. Zhao, Q. Yuan, R. Wang, J. Raj, J. Wu, J. Jiang, and J. Wang, "N-B-OH site-activated graphene quantum dots for boosting electrochemical hydrogen peroxide production," *Advanced Materials*, vol. 35, no. 17, p. 2209086, 2023.

[13] D. Li, Y. Guo, Y. Sun, L. Bai, J. Shi, G. Chen, J. Shi, Y. Liu, C. Jin, Z. Yue, J. Bai, K. Leng, J. Xu, and Y. Qu, "Efficient industrial-current-density H_2O_2 production in neutral medium via external-shell boron regulation on single-atom VN_4 sites," *Chemical Engineering Journal*, vol. 494, no. 15, p. 153211, 2024.

[14] W. Peng, J. Liu, X. Liu, L. Wang, L. Yin, H. Tan, F. Hou, and J. Liang, "Facilitating two-electron oxygen reduction with pyrrolic nitrogen sites for electrochemical hydrogen peroxide production," *Nature Communications*, vol. 14, no. 1, p. 4430, 2023.

[15] Q. Wang, Y. Lei, D. Wang, and Y. Li, "Defect engineering in earth-abundant electrocatalysts for CO_2 and N_2 reduction," *Energy Environmental Science*, vol. 12, pp. 1730-1750, 2019.

[16] Q. Wu, H. Zou, X. Mao, J. He, Y. Shi, S. Chen, R. Yan, L. Wu, C. Lang, B. Zhang, L. Song, X. Wang, A. Du, Q. Li, Y. Jia, J. Chen, and X. Yao, "Unveiling the dynamic active site of defective carbon-based electrocatalysts for hydrogen peroxide production," *Nature Communications*, vol. 14, no. 1, p. 6275, 2023.

[17] X. Shen, Z. Wang, H. Guo, Z. Lei, Z. Liu, and L. Wang, "Solvent engineering of oxygen-enriched carbon dots for efficient electrochemical hydrogen peroxide production," *Small*, vol. 19, no. 43, p. 2303156, 2023.

[18] Y. Bai, D. Deng, J. Wang, Y. Wang, Y. Chen, H. Zheng, M. Liu, X. Zheng, J. Jiang, H. Zheng, M. Yi, W. Li, F. Guozhao, D. Wang, and Y. Lei, "Inhibited passivation by bioinspired cell membrane Zn interface for Zn-air batteries with extended temperature adaptability," *Advanced Materials*, vol. 36, no. 40, p. 2411404, 2024.

[19] T. Wang, Y. Zhang, B. Huang, B. Cai, R. Rao, L. Giordano, S.-C. Sun, and Y. Shao-Horn, "Enhancing oxygen reduction electrocatalysis by tuning interfacial hydrogen bonds," *Nature Catalysis*, vol. 4, no. 9, pp. 753-762, 2021.

[20] Q. Wang, S. Tang, Z. Wang, J. Wu, Y. Bai, Y. Xiong, P. Yang, Y. Wang, Y. Tan, W. Liu, X. Xiong, and Y. Lei, "Electrolyte tuned robust interface toward fast-charging Zn-air battery with atomic Mo site catalyst," *Advanced Functional Materials*, vol. 33, no. 47, p. 2307390, 2023.

[21] P.-Y. Yang, X.-C. Liu, Y.-C. Wang, H.-R. Zheng, J.-X. Wang, J.-Y. Zheng, M.-J. Liu, D.-N. Deng, Y. Bai, Y.-B. Chen, T. Zhang, Z.-M. Liu, and Y. Lei, "The weatherability and heat resistance enhanced by the interaction between AG25 and Mg/Al-LDH," *Rare Metals*, vol. 43, no. 6, pp. 2758-2768, 2024.

[22] J. Shen, X. Qiu, and Y. Zhu, "Nitrogen-doped sp^3 carbon dot catalysed two-electron electrochemical oxygen reduction for efficient production of hydrogen peroxide," *Journal of Materials Chemistry A*, vol. 11, pp. 11704-11711, 2023.

[23] M. Xu, R. Cao, B. Hao, D. Wang, D. Luo, H. Dou, and Z. Chen, "Single-anion conductive solid-state electrolytes with hierarchical ionic highways for flexible zinc-air battery," *Angewandte Chemie International Edition*, vol. 63, no. 36, p. e202407380, 2024.

[24] G.-F. Han, F. Li, W. Zou, M. Karamad, J.-P. Jeon, S.-W. Kim, Y. Bu, Z. Fu, Y. Lu, S. Siahrostami, and J.-B. Baek, "Building and identifying highly active oxygenated groups in carbon materials for oxygen reduction to H_2O_2," *Nature Communications*, vol. 11, no. 1. p. 2209, 2020.

[25] D. Deng, J. Wu, Q. Feng, X. Zhao, M. Liu, Y. Bai, J. Wang, X. Zheng, J. Jiang, Z. Zhuang, X. Xiong, D. Wang, and Y. Lei, "Highly reversible zinc-air batteries at -40°C enabled by anion-mediated biomimetic fat," *Advanced Functional Materials*, vol. 34, no. 2, p. 2308762, 2024.

[26] Y. Wang, Q. Li, M. Wang, H. Ou, D. Deng, H. Zheng, Y. Bai, L. Zheng, Z.-Y. Chen, W. Li, G. Fang, and Y. Lei, "Pumping electrons from oxygen-bridged cobalt for low-charging-voltage

Zn-air batteries," *Nano Letters*, vol. 24, no. 43, pp. 13653-13661, 2024.

[27] T. Prathumsuwan, S. Kladsomboon, A. A. Christy, I. In, X. Liang, S. Song, Y. Wang, T. Inprasit, P. Paoprasert, and N. Sirisit, "Integration of jackfruit seed-derived carbon dots and electronic nose for a sensitive detection of formaldehyde vapor," *Journal of Metals, Materials and Minerals*, vol. 34, no. 1, p. 1846, 2024.

[28] K. Kitsanadecha, C. Sinmak, P. Onchomchan, K. Hantanasirisakul, T. Kwamman, and S. Anantachaisilp, "Synthesis and characterization of electron beam irradiated glutinous rice husk-derived biochar and activated carbon for aqueous electro-chemical capacitors," *Journal of Metals, Materials and Minerals*, vol. 33, no. 3, p. 1687, 2023.

[29] H. Zheng, D. Deng, X. Zheng, Y. Chen, Y. Bai, M. Liu, J. Jiang, H. Zheng, Y. Wang, J. Wang, P. Yang, Y. Xiong, X. Xiong, and Y. Lei, "Highly reversible zn-air batteries enabled by tuned valence electron and steric hindrance on atomic Fe-N$_4$-C Sites," *Nano Letters*, vol. 24, no.15, pp. 4672-4681, 2024.

[30] Y. Wang, J. Wu, S. Tang, J. Yang, C. Ye, J. Chen, Y. Lei, and D. Wang, "Synergistic Fe-Se atom pairs as bifunctional oxygen electrocatalysts boost low-temperature rechargeable Zn-air battery," *Angewandte Chemie International Edition*, vol. 62, no. 15, p. e202219191, 2023.

[31] J. Zhou, P. Yang, P. A. Kots, M. Cohen, Y. Chen, C. M. Quinn, M. D. de Mello, J. A. Boscoboinik, W. J. Shaw, S. Caratzoulas, W. Zheng, and D. G. Vlachos, "Tuning the reactivity of carbon surfaces with oxygen-containing functional groups," *Nature Communications*, vol. 14, no. 1, p. 2293, 2023.

[32] H. Wu, W. Yuan, L. Li, X. Gao, Z. Zhang, and Y. Qian, "Ultra-high capacity and stable dual-ion batteries with fast kinetics enabled by HOF supermolecules derived 3D nitrogen-oxygen Co-doped nanocarbon anodes," *Advanced Functional Materials*, vol. 34, no. 46, p. 2406540, 2024.

[33] S. Chen, T. Luo, K. Chen, Y. Lin, J. Fu, K. Liu, C. Cai, Q. Wang, H. Li, X. Li, J. Hu, H. Li, M. Zhu, and M. Liu, "Chemical identification of catalytically active sites on oxygen-doped carbon nanosheet to decipher the high activity for electro-synthesis hydrogen peroxide," *Angewandte Chemie International Edition*, vol. 60, no. 30, pp. 16607-16614, 2021.

[34] K. Lee, J. Lim, M. J. Lee, K. Ryu, H. Lee, J. Y. Kim, H. Ju, H.-S. Cho, B.-H. Kim, M. C. Hatzell, J. Kang, and S. W. Lee, "Structure-controlled graphene electrocatalysts for high-performance H$_2$O$_2$ production," *Energy Environmental Science*, vol. 15, no. 7, pp. 2858-2866, 2022.

[35] Q. Wang, Q. Feng, Y. Lei, S. Tang, L. Xu, Y. Xiong, G. Fang, Y. Wang, P. Yang, J. Liu, W. Liu, and X. Xiong, "Quasi-solid-state Zn-air batteries with an atomically dispersed cobalt electro-catalyst and organohydrogel electrolyte," *Nature Communications*, vol. 13, p. 3689, 2022.

[36] H. Zheng, S. Wang, S. Liu, J. Wu, J. Guan, Q. Li, Y. Wang, Y. Tao, S. Hu, Y. Bai, J. Wang, X. Xiong, Y. Xiong, and Y. Lei, "The heterointerface between Fe$_1$/NC and selenides boosts reversible oxygen electrocatalysis," *Advanced Functional Materials*, vol. 33, no. 40, p. 2300815, 2023.

[37] P. Yang, X. Liu, Z Liu, T. Zhang, H. Zheng, H. Ou, Y. Wang, Y. Bai, M. Liu, D. Deng, J. Wang, Y. Chen, H. Zheng, J. Jiang, and Y. Lei, "Hyperspectral and weather resistant biomimetic leaves enabled by interlayer confinement," *Advanced Functional Materials*, vol. 34, no. 45, p. 2405908, 2024.

[38] X. Li, X. Wang, G. Xiao, and Y. Zhu, "Identifying active sites of boron, nitrogen co-doped carbon materials for the oxygen reduction reaction to hydrogen peroxide," *Journal of Colloid and Interface Science*, vol. 602, no, 15, pp. 799-809, 2021.

[39] Q. Zhang, H. Che, H. Yang, B. Liu, and Y. Ao, "Tandem proton transfer in carboxylated supramolecular polymer for highly efficient overall photosynthesis of hydrogen peroxide," *Angewandte Chemie International Edition*, vol. 63, no. 38, p. e202409328, 2024.

[40] Y. Yang, Q. Guo, Q. Li, L. Guo, H. Chu, L. Liao, X. Wang, Z. Li, and W. Zhou, "Carbon quantum dots confined into covalent triazine frameworks for efficient overall photocatalytic H$_2$O$_2$ production," *Advanced Functional Materials*, vol. 34, no. 29, p. 2400612, 2024.

[41] D. Deng, Y. Wang, J. Jiang, Y. Bai, Y. Chen, H. Zheng, H. Ou, and Y. Lei, "Indium oxide with oxygen vacancies boosts O$_2$ adsorption and activation for electrocatalytic H$_2$O$_2$ production," *Chemical Communications*, vol. 60, no. 70, pp. 9364-9367, 2024.

[42] L. Du, Q. Tian, X. Zheng, W. Guo, W. Liu, Y. Zhou, F. Shi, and Q. Xu, "Supercritical CO$_2$-tailored 2D oxygen-doped amorphous carbon nitride for enhanced photocatalytic activity," *Energy Environmental Materials*, vol. 5, no. 3, pp. 912-917, 2022.

[43] Z. Bao, J. Zhao, S. Zhang, L. Ding, X. Peng, G. Wang, Z. Zhao, X. Zhong, Z. Yao, and J. Wang, "Synergistic effect of doped nitrogen and oxygen-containing functional groups on electro-chemical synthesis of hydrogen peroxide," *Journal of Materials Chemistry A*, vol. 10, no. 9, pp. 4749-4757, 2022.

[44] Y. Chen, C. Zhen, Y. Chen, H. Zhao, Y. Wang, Z. Yue, Q. Wang, J. Li, M. D. Gu, Q. Cheng, and H. Yang, "Oxygen functional groups regulate cobalt-porphyrin molecular electrocatalyst for acidic H$_2$O$_2$ electrosynthesis at industrial-level current," *Angewandte Chemie International Edition*, vol. 63, no. 34, p. e202407163, 2024.

[45] T. Xu, Z. Wang, W. Zhang, S. An, L. Wei, S. Guo, Y. Huang, S. Jiang, M. Zhu, Y.-B. Zhang, and W.-H. Zhu, "Constructing photocatalytic covalent organic frameworks with aliphatic linkers," *Journal of the American Chemical Society*, vol. 146, no. 29, pp. 20107-20115, 2024.

[46] J. Zhang, M. Li, Z. Liu, J. Lian, Y. Huang, Z. Sun, and Z. Qiang, "Polyacrylamide degradation in oil field wastewater by UV/H$_2$O$_2$ and UV/PDS: Rapid experimental measurement and model simulation," *Chemical Engineering Journal*, vol. 485, no. 1, p. 149745, 2024.

[47] A. Tufail, J. Al-Rifai, W. E. Price, J. P. V. D. Merwe, F. D. L. Leusch, and F. I. Hai, "Elucidating the performance of UV-based photochemical processes for the removal of trace organic contaminants: Degradation and toxicity evaluation," *Chemosphere*, vol. 350, p.140978, 2024.

[48] L. Cui, M. Sun, and P. Z. Zhang, "An efficient, green, and residual oxidant-free wastewater treatment technique enabled by coupling a dual-cathode heterogeneous electro-Fenton process and UV lradiation in tandem," *Green Chemistry*, vol. 25, pp. 6315-6326, 2023.